First-principles rationalization of self-reduction and lanthanide defect levels in SrB$_4$O$_7$

Haoming Xu [1,2] Weiguo Jing,[1,2,*] Mingzhe Liu,[1,2] Min Yin,[1] and Chang-Kui Duan [1,2,†]

[1]*CAS Key Laboratory of Microscale Magnetic Resonance, and School of Physical Sciences,*
University of Science and Technology of China, Hefei 230026, China
[2]*CAS Center for Excellence in Quantum Information and Quantum Physics,*
University of Science and Technology of China, Hefei 230026, China

The "abnormal" self-reduction of several trivalent lanthanides in borates has been reported for a couple of decades, especially in SrB$_4$O$_7$, but only a phenomenological explanation has been given. Our calculations of the formation energies of lanthanide-doped and intrinsic defects in SrB$_4$O$_7$ provide an explanation for the mechanisms of self-reduction phenomena. Furthermore, we also give the trends of the $4f$ and $5d$ host referred binding energies of divalent lanthanides, which well fits and supports the result based on the extrapolation of the experimental data with the semiempirical chemical shift model [P. Dorenbos, Phys. Rev. B **85**, 165107 (2012)]. Our results show that the calculations based on the supercell method by employing the projector augmented wave pseudopotentials are capable of interpreting the reduction and charge-transfer phenomena, and can provide a basis for the design of lanthanide-doped optical materials.

I. INTRODUCTION

Borate systems with the versatility of efficient luminescence have attracted broad attention because of their applications in fluorescent lamps, display devices, detector systems represented by x-ray screens, immunoassays, and scintillates of phosphor marking. Furthermore, as a main branch of borate systems, inorganic borates are widely investigated as important host matrices of phosphors, due to their strong covalent bonds and large band gaps. For example, the lanthanide-doped strontium tetraborate SrB$_4$O$_7$:Ln (Ln = La–Lu) has been studied as a potential nonlinear optical material with some excellent mechanical and optical properties, such as high mechanical strength, nonhygroscopicity, and high optical damage threshold.

Lanthanides usually exist as trivalent ions in oxides synthesized in the air atmosphere, and the reduction of trivalent lanthanide ions to their divalent ones generally requires a strong reducing agent. However, it is known that SrB$_4$O$_7$ has the unique property of stabilizing divalent Eu, Sm, and Yb without any reducing agent when prepared at 700−900 °C (typically 850°C) [1–5]. Other experiments reported that divalent Tm, Nd, and Dy in SrB$_4$O$_7$ can also be synthesized in air at a lower preparation temperature (650°C) [6–8]. Such "abnormal" reduction of Ln^{3+} to Ln^{2+} in a nonreduction atmosphere was attributed to the closely surrounded tetrahedral BO$_4$ anion network in the host structure [2]. A deeper understanding of this self-reduction via first-principles calculations should help us design lanthanide-doped optical materials not limited to borate systems.

The charge-transfer (CT) transitions are significant in lanthanide-doped materials, usually appearing in the absorption or excitation spectrum in experiments. A semiempirical chemical shift model has been developed by Dorenbos [9,10] based on summarizing a large amount of CT and $4f$–$5d$ transition energies of lanthanides from experiments. This semiempirical model illustrates that the binding energies of an electron in lanthanide $4f^n$ states vary with n in a characteristic zigzag shape that is almost independent of the type of compound. The variation is anticorrelated with the known variation in $4f$–$5d$ transition energies in divalent lanthanides. Because of the anticorrelation, the energy differences between the first $4f^{n-1}5d$ state and the conduction band minimum (CBM) are relatively invariant with the type of lanthanide ion. With the parameters summarized in the model, the $4f$ and $5d$ curves can be easily obtained in a given compound, once the defect levels of one lanthanide are available according to experiments. It can be used to predict the CT transition energies and associated $4f$ and $5d$ binding energies of the whole lanthanide series referenced to the valence band maximum (VBM). Although some systematic first-principles investigations have been reported to study the electronic structure and magnetic properties of LnNiO$_2$ [11] and the defect levels induced by lanthanides in GaN:Ln [12] (Ln = La–Lu), the trends of CT levels and the binding energies of lanthanide dopants have scarcely been reported systematically in insulators via first-principles calculations.

The first-principles calculations based on the density-functional theory (DFT) with the supercell method by employing the projector augmented wave (PAW) pseudopotentials [13,14] have been proven to be a useful tool to study the optical properties of intrinsic scintillators in general, but lanthanides with partially filled $4f$ states are often incorrectly described by the presently available PAW pseudopotentials

*jingwg@mail.ustc.edu.cn
†ckduan@ustc.edu.cn

due to self-interaction errors of $4f$ electrons. A routine way to cope with the inabilities of present density functionals to describe the localized $4f$ electrons of lanthanides is to place the $4f$ electrons in the core. However, since the study here involves the change in the occupancy of $4f$ orbitals, the PAW pseudopotentials in which the $4f$ states are treated as valence states should be employed. The electronic correlation effects are carefully considered by introducing on-site Coulomb interactions or employing hybrid functionals.

The purpose of this paper is to identify the underlying factors that affect the stability of Ln^{2+} in SrB_4O_7 by exploring the most significant defects of the pristine host and the defects formed by doping lanthanide ions. Furthermore, the CT transitions involving $4f$ and $5d$ electrons will also be calculated and compared with experimental data and Dorenbos' semiempirical model.

II. METHODS

A. Formation energy and chemical potential

The more energy that is required the more difficult it is to form a defect. The formation energy of a defect X in the net charge state of q is defined as [15]

$$E^f[X^q] = E_{tot}[X^q] - E_{tot}[bulk]$$
$$- \sum_i n_i\,\mu_i + q(E_F + E_{VBM}), \quad (1)$$

where $E_{tot}[X^q]$ and $E_{tot}[bulk]$ are the total energies derived from a supercell containing the defect (with necessary corrections included) and the pristine host, respectively, n_i is the change in the number of type i atom species, which is added to ($n_i > 0$) or removed from ($n_i < 0$) the perfect supercell, μ_i is the corresponding chemical potential for type i atom species, E_F is the electron Fermi level of the defect system referenced to the VBM in the bulk, and E_{VBM} is the energy of the VBM in the bulk, which need to be explicitly included in this expression due to the choice of this reference of the E_F. The *post hoc* corrections including both image-charge interaction correction (E_{IIC}) and potential alignment correction ($q\Delta V_{NAP}$) have been included in the total energy of charged defects ($E_{tot}[X^q]$), following the method proposed in Ref. [16], which can be extended to anisotropic dielectrics and noncubic cells.

The chemical potentials in Eq. (1) are subject to the influence of partial pressures, temperature, and a series of thermodynamic constraints under the equilibrium growth condition. The chemical potential of oxygen can be expressed as [17]

$$\mu_O = \frac{1}{2}E[O_2] + \frac{1}{2}k_BT\left[\ln\left(\frac{pV_Q}{k_BT}\cdot\frac{\sigma B_0}{k_BT}\right) - \ln Z_{vib}\right]$$
$$= \mu_O^0 + \Delta\mu_O, \quad (2)$$

where $E[O_2]$ is the total energy of a spin-triplet O_2 molecule, k_B is the Boltzmann constant, T is the temperature, p is the partial pressure of oxygen, $V_Q = (h^2/2\pi mk_BT)^{3/2}$ is the quantum volume, h is the Planck's constant, $m = 31.998$ AMU (atomic mass unit) is the mass of an O_2 molecule, $\sigma = 2$ for O_2 is the associated symmetry factor, the rotation constant of O_2 is $B_0 = 1.44$ cm^{-1} in energy, and

Z_{vib} is the vibrational partition function whose contribution to the chemical potential is usually very small and ignored. We rewrite the chemical potentials of each element in terms of $\Delta\mu$ relative to the chemical potential of the elementary substance, e.g., $\Delta\mu_O$ is relative to $\mu_O^0 = \frac{1}{2}E[O_2]$.

If a defect reaches thermodynamic equilibrium distribution at temperature T in a thorough chemical reaction, its concentration can be related to the formation energy as an approximation to the Gibbs energy of formation with the following expression [15]:

$$c[X^q] = N\omega\exp\left(-\frac{E^f[X^q]}{k_BT}\right), \quad (3)$$

where N is the concentration of potential atomic sites for the defect to reside in the solid, ω is an additional degeneracy-related factor of the defect, and $E^f[X^q]$ is the formation energy calculated by Eq. (1). Hence, a larger formation energy indicates an exponentially smaller concentration of the defect, and vice versa.

The Fermi level in a thermodynamic context depends on any defects or impurities contained therein and is determined by the condition of charge neutrality [17], i.e.,

$$\sum_{X,q} q\,c[X^q] + n_h - n_e = 0, \quad (4)$$

where n_h and n_e are the concentrations of free holes in the valence band (VB) and free electrons in the conduction band (CB), respectively. For the large band gap of SrB_4O_7 with E_F sufficiently far from the gap edges, both n_h and n_e are small and routinely neglected.

B. Charge transition level and charge-transfer transition energy

The thermodynamic charge transition level (CTL) of a defect X between charge states q_1 and q_2 (taking $q_1 > q_2$) is defined as the Fermi level of the defect system when the formation energies of defect X in charge states q_1 and q_2 are equal at their corresponding equilibrium geometric structures [15],

$$X(q_1/q_2) = \frac{E_{tot}[X^{q_1}] - E_{tot}[X^{q_2}]}{q_2 - q_1} - E_{VBM}. \quad (5)$$

The CTL provides a criterion for determining the charge state of defects. When the Fermi level E_F is lower than $X(q_1/q_2)$, the higher charge state q_1 of the defect X is more stable and dominant than charge state q_2, and vice versa.

The adiabatic CT transition energy (denoted as $E_{CT}^0[X^q]$) of an electron from the VBM to the dopant can be related to the value of CTL as follows:

$$E_{CT}^0[X^q] \approx E_{tot}[X^{q-1}] - (E_{tot}[X^q] + E_{VBM})$$
$$\approx X(q/(q-1)), \quad (6)$$

where E_{VBM} is approximately the energy of an electron at the VBM. Experimentally, $E_{CT}^0[X^q]$ can be related to the onset of the CT band in the excitation or absorption spectrum. However, generally the CT band is very broad and extended whose onset might be barely determined. Then a peak or, occasionally, a slope at the low-energy side is experimentally determined.

The Kröger-Vink notation D_S^C is used to describe the net charge C ($\prime$, $\times$, $\bullet$ being -1, 0, and $+1$, respectively) and lattice site S of a dopant D. In particular, $D = V$ means a vacancy and $S = i$ means an interstitial site. Taking Eu_{Sr} as an example, $E_{CT}^0[Eu_{Sr}^\bullet] \approx Eu_{Sr}(+1/0)$ is an approximation of the adiabatic transfer of an electron from VB to Eu^{3+} ($q = 1$ relative to Sr^{2+}, the ion originally at the lattice site) to form Eu^{2+} ($q = 0$). Unless otherwise stated, the CTL in the following refers specifically to $Ln_{Sr}(+1/0)$ for different lanthanides, as we mainly focus on the charge transition between the trivalent and divalent states.

C. Computational details

The first-principles calculations based on DFT are performed using the Vienna *ab initio* simulation package (VASP) [18,19], by employing the Perdew-Burke-Ernzerhof revised for solids (PBEsol) [20] exchange-correlation functional within the generalized gradient approximation (GGA) [21]. The spin-polarized calculations are carried out with the PAW pseudopotentials for interactions of atoms, which are obtained from the VASP database for all the elements involved in the calculations, as recommended in the VASP manual, while for lanthanides the $4f$ and $5d$ states are included as valence electrons.

The conjugate-gradient algorithm is used for the unit cell to perform the geometric structure optimizations (ionic positions, cell volume, and cell shape are all allowed to relax), with a Γ-centered $3 \times 8 \times 8$ k-point grid and an energy cutoff for the plane-wave-basis set of 520 eV, until the energy change less than 10^{-5} eV and the maximum Hellmann-Feynman force exerted on each atom is less than 0.01 eV/Å.

We construct a $1 \times 2 \times 2$ supercell from the equilibrium unit cell for lanthanide-doped defect calculations. Only one Γ k-point is used to sample the Brillouin zone for calculations on the supercell with an energy cutoff of 400 eV. The lattice parameters are fixed during the structure relaxations of defects in the supercell. We have performed convergence tests by calculating the defect supercell using a Γ-centered $3 \times 3 \times 3$ k-point grid or using 520 eV energy cutoff. Compared with the results of the single Γ point and 400 eV energy cutoff, the changes in total energy differences are less than 0.02 eV and 0.016 eV for the $3 \times 3 \times 3$ k-point grid and 520 eV energy cutoff, respectively (more details in Tables S1 and S2 within the Supplemental Material [22]). The tests show that the Γ-point sampling and 400 eV energy cutoff are sufficient enough for the supercell in our calculations.

The differences in electron localization between the element in a molecule and that in solids can result in substantial errors due to the overbinding of molecules of elements that take on negative oxidation states in solids in GGA calculated formation energies [23]. Therefore, the anion corrections have been adopted for the elementary substances (by adding 1.38 eV per O_2 molecule in this case) in chemical potential calculations.

For lanthanide atoms, the electron-electron correlation effect is important for the localized $4f$ orbitals. Therefore, the Hubbard on-site correction (GGA + U) with the rotationally invariant approach [21] is applied only to lanthanide atoms in the GGA calculations. In order to compare the series of lanthanides, the Hubbard U parameters are all set the same as 6 eV for the $4f$ orbitals of all lanthanide atoms, similar to the previous GGA + U study on lanthanide-doped systems [24,25]. We have tested the impact of different U values in the range of 4–8 eV, which is little on the local structure, but the CTLs depend weakly on U values almost linearly. Compared to the case of the chosen intermediate value of 6 eV, the changes in CTLs calculated with the lower value of $U = 4$ eVeV and the upper value of $U = 8$ eV are within 0.2 eV, with detailed test results in Figs. S8 and S9 within the Supplemental Material [22].

As the band gap of insulators is substantially underestimated by the GGA method in general, in order to obtain the CTLs in the correct band gap, we perform the dielectric-dependent hybrid functional calculations based on the Perdew-Burke-Ernzerhof functional (PBE0-α) [26,27] in the supercell, starting from the structure obtained by the GGA + U method and relaxing the atomic positions while the lattice parameters are fixed. The fraction of exact exchange (denoted as α) in the PBE0-α calculations is determined via $\alpha = 1/\varepsilon_\infty = 0.31$, where the high-frequency dielectric tensor ε_∞ is calculated in the independent-particle approximation (including local field effects in DFT) by means of density functional perturbation theory [28,29] with the GGA method. The PBE0-α functional contains α of the exact exchange and $(1 - \alpha)$ of the PBE exchange, and all the PBE correlation energy. Therefore, it can also handle the exchange-correlation interactions without resorting to the Hubbard U correction.

A constrained occupancy approach is applied to the equilibrium configurations of the excited states of lanthanides. All the excited states involved in the results are confirmed to be properly occupied by checking the site projected wave function character of each orbital. The constrained occupancy approach is failed to obtain the $4f^{n-1}5d$ states of Pr^{2+} to Sm^{2+} and the $4f^n$ states of La^{2+}, Ce^{2+}, and Gd^{2+} with the PBE0-α method due to the switch of orbital orders typically occurring when the occupancy is changed. All the $4f^{n-1}5d$ states we calculated are the lowest-energy high-spin states, which are generally approximated by a single determinant within the DFT, and the direct and exchange Coulomb interactions should have been automatically included in the density functional calculation approximately.

The spin-orbit coupling is not introduced in the above calculations as it is not important for SrB_4O_7. For lanthanides with $4f^n$ and $4f^{n-1}5d$ configurations, as the $4f$ electrons are not handled well due to the self-interaction errors according to the VASP manual, the reliability of the calculations that introduce the spin-orbit coupling interaction associated with $4f$ electrons is insufficient. On the other hand, the $4f$ electrons of lanthanides are strongly localized and less affected by the surrounding environment. Therefore, the spin-orbit coupling is weakly host-dependent and can be included more conveniently (and reliably as well) by a *post hoc* correction to the multiplet state $^{2S+1}L_J$ of the $4f^n$ configuration (and the $4f^{n-1}$ core of the $4f^{n-1}5d$ configuration) with the highest-spin quantum number as follows [31]:

$$\Delta E_{SOC} = \eta \frac{\zeta}{2S} \frac{J(J+1) - S(S+1) - L(L-1)}{2}, \quad (7)$$

TABLE I. Spin-orbit coupling corrections to lanthanides.

	La	Ce	Pr	Nd	Pm	Sm	Eu
ζ^a (eV)	0.07	0.08	0.09	0.11	0.12	0.14	0.17
ΔE^b (eV)	−0.13	−0.08	−0.05	0.00	0.06	0.14	0.33
	Gd	Tb	Dy	Ho	Er	Tm	Yb
ζ^a (eV)	0.19	0.21	0.24	0.26	0.29	0.32	0.36
ΔE^b (eV)	−0.28	−0.21	−0.12	0.00	0.15	0.32	0.54

[a]Reference [30].

[b]The ΔE refers to the spin-orbit coupling corrections to the CTL of the $4f^{n-1}/4f^n$ configurations for $Ln^{3+/2+}$ ($n = 1$) to $Yb^{3+/2+}$ ($n = 14$).

where the sign η is $+1$ for the first half of the $4f$ shell ($n \leqslant 7$) or -1 for the second half, and ζ is the spin-orbit coupling constant, whose quasi-free-ion values in a host are only weakly host-dependent and taken from Ref. [30]. For the $4f^n$ configurations ($n = 0 \sim 14$), the lowest states $^{2S+1}L_J$ are $^1S_0$, $^2F_{5/2}$, $^3H_4$, $^4I_{9/2}$, $^5I_4$, $^6H_{5/2}$, $^7F_0$, $^8S_{7/2}$, $^7F_6$, $^6H_{15/2}$, $^5I_8$, $^4I_{15/2}$, $^3H_6$, $^2F_{7/2}$, and $^1S_0$, respectively. The specific correction values to CTL of $4f^{n-1}/4f^n$ configurations are listed in Table I, and more details are listed in Tables S4 and S5 within the Supplemental Material [22].

III. RESULTS AND DISCUSSION

A. Host properties

Figure 1 shows the crystal structure of the SrB_4O_7 orthorhombic unit cell (space group $Pmn2_1$, no. 31) and the coordination environments of Sr^{2+} and B^{3+}. The coordination numbers of Sr^{2+} and B^{3+} ions are 4 and 9, respectively. The lattice parameters of the unit cell are obtained with the GGA method. The Perdew-Burke-Ernzerhof exchange-correlation functional overestimates the lattice parameters by $\sim$1%, while the results of the PBEsol exchange-correlation functional ($a = 10.729$ Å, $b = 4.426$ Å, $c = 4.235$ Å) deviate from the experimental data [32–35] by only 0.2%. Hence, the PBEsol exchange-correlation functional is used for the results presented hereafter.

The calculation based on the Kohn-Sham (KS) eigenvalues with the GGA method produces a substantially underestimated indirect band gap energy of 7.16 eV for the pure SrB_4O_7 host, while the PBE0-α ($\alpha = 0.31$) method predicts
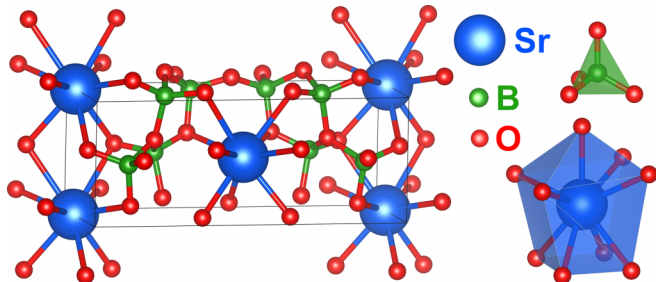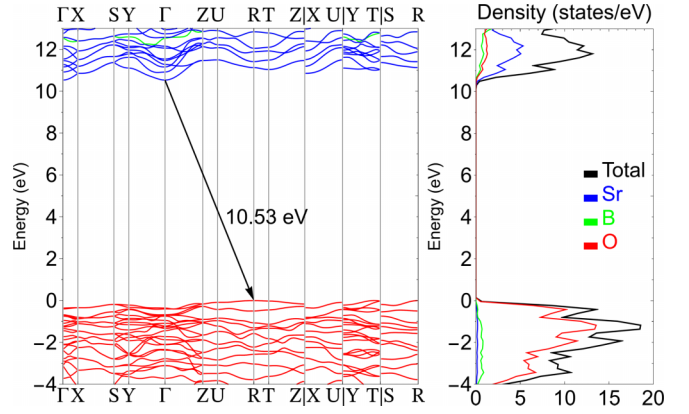

FIG. 2. Band structure (left) and density of states (right) of SrB_4O_7 calculated with the PBE0-α method.

an improved generalized KS band gap energy of 10.53 eV (Fig. 2). The VBM obtained with two different methods is aligned by identifying the common average electrostatic potential energy felt by an electron in the pristine host. Relative to the values obtained with the GGA method, the energy of the VBM obtained with the PBE0-α method shifts downward by ΔVBM = 2.15 eV, and the energy of the CBM obtained with the PBE0-α method shifts upward by ΔCBM = 1.22 eV (more details are plotted in Fig. S1 within the Supplemental Material [22]).

Several experiments report that the zero transmission of the SrB_4O_7 crystal is reached at 130 nm (9.54 eV) [33], 124 nm (10.00 eV) [36], and even below 120 nm (10.33 eV) [34], and the band gap energy from excitation spectra in SrB_4O_7:Sm is higher than 10 eV [37]. These values indicate that the band gap obtained with the PBE0-α method is reasonable, and therefore the VBM obtained with the PBE0-α method, rather than that obtained with the GGA method, is chosen as the energy reference of the Fermi level.

The CB and VB are mainly of Sr–d and O–p characters, respectively. The influence of the spin-orbit coupling of Sr to the CB is shown to be negligible in our calculation.

B. Intrinsic defects

The limiting bounds and variable region of the chemical potential [Fig. 3(a)] to sustain the SrB_4O_7 host is predominantly shaped by $Sr_3B_2O_6$ and SrB_8O_{13}. In the variable region, the chemical environment is mainly characterized by the chemical potential of O. To simulate the air atmosphere in experiments, $\Delta\mu_O$ is set as -1.3 eV, determined by the chemical potential of O_2 in the air at 1123 K and 0.21 atm using Eq. (2), while $\Delta\mu_{Sr}$ and $\Delta\mu_B$ are set as the corresponding intermediate values.

The formation energies of intrinsic defects are calculated with the GGA method for the consideration of computational costs, and the PBE0-α band edges are also indicated in Fig. 3 for illustrative purposes only. We consider vacancies and interstitials of Sr, B, and O ions, as well as the antisite defects between them. Each isolated single defect is modeled by adding an atom to, removing an atom from, or replacing an atom with another atom in a pristine supercell that contains 8 Sr, 32 B, and 56 O atoms.
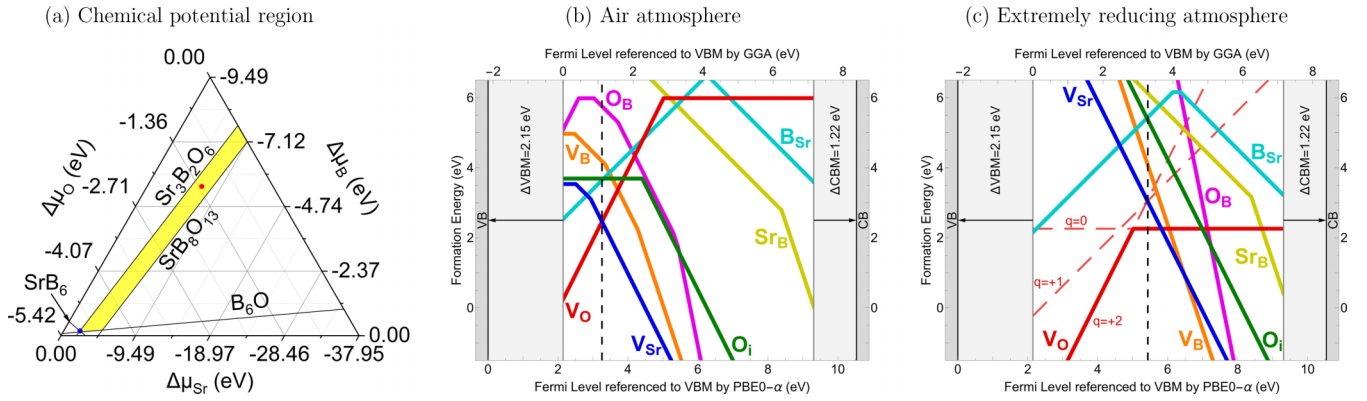

FIG. 1. Crystal structure of orthorhombic SrB_4O_7 and coordination environments of Sr^{2+} and B^{3+}.

FIG. 3. Limiting bounds and the variable region (yellow) for the chemical potential (a) of each element to sustain the SrB_4O_7 host. Formation energy vs Fermi level for intrinsic defects of SrB_4O_7 host in the air atmosphere (b) with $\Delta\mu_O = -1.30$ eV and extremely reducing atmosphere (c) with $\Delta\mu_O = -5.03$ eV, in which the equilibrium Fermi levels (vertical dashed line) are 3.26 eV and 5.43 eV referenced to the VBM (PBE0-α), respectively.

The poly-lines of the formation energies of various potentially important defects are shown in Fig. 3(b) for the air atmosphere (with $\Delta\mu_O = -1.30$ eV) and Fig. 3(c) for the extremely reducing atmosphere (with $\Delta\mu_O = -5.03$ eV). The equilibrium Fermi level (E_F^{eq}) can be determined with the charge neutrality condition by Eq. (4) once the chemical potentials are specified. Schematically, it is approximately located at the intersection of the one leading positively-charged defect and one leading negatively-charged defect in the diagram of E^f versus E_F for all potentially important defects, and the formation energy of a defect is approximately the intersection of the E^f poly-line and the vertical dashed line at the E_F^{eq}.

The interstitials Sr_i, B_i, and antisite B_O, etc. are of very high formation energies and negligible concentrations, and therefore are not plotted in the figure for clarity. Figure 3(b) shows that in the air atmosphere the dominant defects are the vacancies V_{Sr}'' and $V_O^{\bullet\bullet}$ with the fractional concentrations of $\sim 9 \times 10^{-12}$ estimated by $\exp(-E^f/k_B T)$. In the extremely reducing atmosphere [Fig. 3(c)], the E_F^{eq} shifts to higher energy, and the dominant defect is $V_O^\times$ with the fractional concentrations of $\sim 7 \times 10^{-11}$.

C. Self-reduction of trivalent lanthanide ions

Lanthanide ions are substituted to the site of Sr to simulate a lanthanide-doped system, as the substitutions of lanthanide ions for B or O sites are not favorable because of the difference in ion radius and charge mismatch. The formation energies are calculated with the GGA + U method for lanthanide-related defects, and with the GGA method for intrinsic defects. Figure 4 shows the formation energies versus Fermi level for defects involving lanthanide (Eu) doping in the air atmosphere. Only the formation energy of Eu_{Sr} and those dominant defects are plotted in Fig. 4, while the other lanthanides are marked with dots to indicate the CTLs of the Ln_{Sr} defects. The doping concentration is approximately 1% by controlling the chemical potential of lanthanide at a suitable value with Eq. (3). The concentration of the dominant negatively-charged intrinsic defect V_{Sr}'' in the undoped sample is so low that the existence of $Eu_{Sr}^\bullet$ leads to a greatly upshifted equi-

librium Fermi level $E_F^{eq\,\prime} = 3.95$ eV referenced to the VBM (PBE0-α).

For illustrative purposes, the poly-line of the Eu_{Sr} defect can shift up and down according to the doping concentration, but it cannot shift below the lower parallel dotted line, which is the lower limit of the formation energy of the Eu_{Sr} defect, determined by the extremely Eu rich condition at the coexistence of SrB_4O_7, Eu_2O_3, and O_2. Alternatively, it can shift left and right as the type of lanthanide changes, simply by adjusting the abscissa of the turning point a of $q = +1$ and $q = 0$ to the corresponding CTL position of another lanthanide. The point c in Fig. 4 is the intersection of the leading negatively-charged defect V_{Sr}'' and the leading positively-charged $Eu_{Sr}^\bullet$ ($q = +1$) defect, whose abscissa is approximately the position of the equilibrium Fermi level ($E_F^{eq\,\prime}$). For example, if we replace 1% Eu with 1% Yb, the $E_F^{eq\,\prime}$ will increase by 0.11 eV.
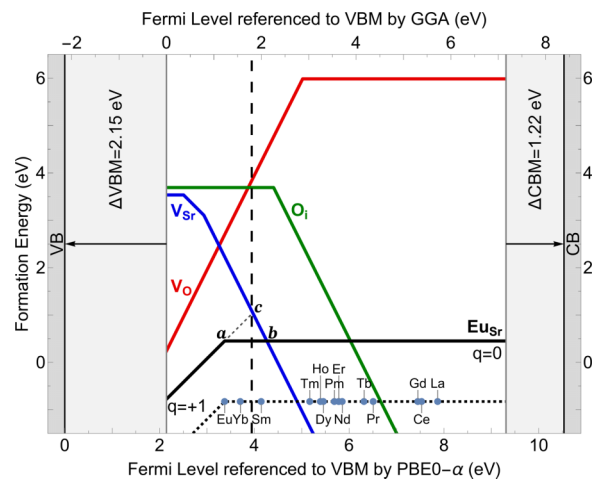

FIG. 4. Formation energy vs Fermi level for 1% lanthanide-doped defects of SrB_4O_7 host in the air atmosphere. Europium is taken as an example of lanthanides, in which case the equilibrium Fermi level is 3.95 eV referenced to the VBM (PBE0-α). The lower limit of the formation energy determined by the extremely Eu-rich condition is indicated by the parallel dotted line below, on which the positions of the (+1/0) CTLs for Ln_{Sr} defects are marked with dots.
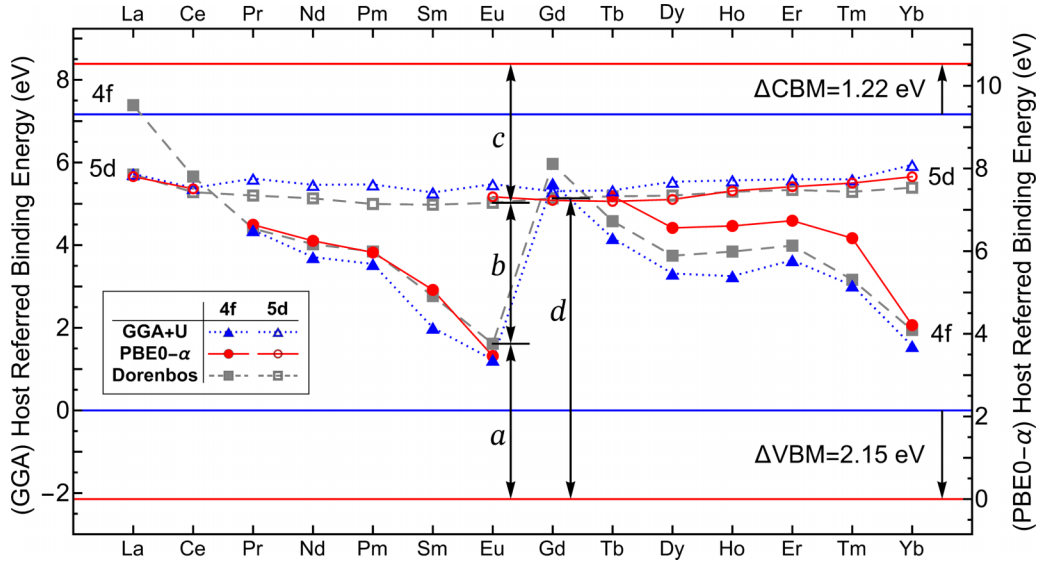
FIG. 5. Host referred binding energies for $4f^n$ (solid symbol, marked with $4f$) and $4f^{n-1}5d$ (open symbol, marked with $5d$) levels of divalent lanthanide ions doped in SrB_4O_7. The dotted (triangle, blue), solid (circle, red), and dashed (square, gray) curves are the results of GGA + U, PBE0-α and Dorenbos' semiempirical model, respectively. Calculations for the $4f^{n-1}5d$ states of Pr^{2+} to Sm^{2+} and the $4f^n$ states of La^{2+}, Ce^{2+}, and Gd^{2+} with the PBE0-α method are failed. The zero of energy on the left-hand side is at the VBM obtained with the GGA method, while the zero of energy on the right-hand side is at the VBM obtained with the PBE0-α method. The a, b, c, and d represent different transition processes and are explained in detail in the main text.

Furthermore, the dominant valence of a dopant lanthanide can be predicted by the relative position of the CTL of the corresponding lanthanide to the point b in Fig. 4, which is the intersection of the leading negatively-charged defect V_{Sr}'' and the uncharged $Eu_{Sr}^{\times}$ ($q = 0$) defect. For a given doping concentration and chemical condition, those lanthanide ions with CTLs to the left of the point b are mainly divalent, while other lanthanide ions with CTLs to the right of the point b are mainly trivalent. That is because if the point a (CTL) is to the left of point b, then the abscissa of the intersection point c must be between the point a ($E_F^{eq\,\prime}$) and b, resulting in the $E_F^{eq\,\prime}$ above the CTL. In the experimental condition of 1% doping concentration, 1123 K and the air atmosphere in Fig. 4, the $E_F^{eq\,\prime}$ is above the CTL $Ln_{Sr}(+1/0)$ for Ln = Eu, Yb, and Sm-doped systems, and therefore the neutral $Ln_{Sr}^{\times}$ forms, i.e., the doped lanthanide ions are mainly divalent. These results provide an explanation for the unique property of stabilizing Eu^{2+}, Yb^{2+} and Sm^{2+} doped in SrB_4O_7 prepared in the air atmosphere without any reducing agent reported in experiments [1–5].

In addition, Xu *et al.* reported that some Ln^{2+} ions turned up by preparing the Ln-doped SrB_4O_7 in the air at 650 °C for Ln = Tm [6], Nd [7], and Dy [8], while the signature of divalent Ln^{2+} disappeared when the samples were prepared in the air at 900 °C. This might be related to the incomplete solid-state phase reaction in which the system has not achieved chemical equilibrium at a lower temperature. For example, the part of the sample with the accumulation of Ln^{3+} ions requires a large concentration of V_{Sr}'' to compensate, which means higher local E_F and the appearance of a tiny fractional concentration of divalent lanthanides. A trace amount of divalent lanthanides can be detected in experiments

by the strong $4f \leftrightarrow 5d$ transition. To achieve a substantial proportion of divalent lanthanide ions in the host, a higher $E_F^{eq\,\prime}$ is needed, which can be realized by preparing the sample in a more reducing atmosphere.

D. Host referred binding energy

Here, the host referred binding energy (HRBE) of the $4f^n$ ground state, referred to as the $4f$ level hereafter, is defined as the minimum energy required to adiabatically transfer an electron from the VBM to a Ln^{3+} ion to form a Ln^{2+} ion of the $4f^n$ configuration (arrow a in Fig. 5). Alternatively, it can be related to the energy released when a hole in the host is trapped by the $4f^n$ Ln^{2+} ion. The initial and final states of this process are a Ln^{3+} ($4f^{n-1}$) ion with an electron at the VBM and a Ln^{2+} ($4f^n$) ion, respectively. Approximating the energy of an electron at the VBM as E_{VBM}, we can calculate the $4f$ level by

$$\text{HRBE}(4f) = E_{tot}[Ln^{2+}(4f^n)] \\ - \{E_{tot}[Ln^{3+}(4f^{n-1})] + E_{VBM}\}, \tag{8}$$

which is similar to Eq. (6). The HRBE of the lowest energy high-spin $4f^{n-1}5d$ state of Ln^{2+}, referred to as the $5d$ level hereafter, is similarly defined. For La, Ce and Gd, the ground state is the $4f^{n-1}5d$ state (arrow d in Fig. 5), so we can calculate the $5d$ level similarly by

$$\text{HRBE}(5d) = E_{tot}[Ln^{2+}(4f^{n-1}5d)] \\ - \{E_{tot}[Ln^{3+}(4f^{n-1})] + E_{VBM}\}. \tag{9}$$

For the other lanthanides, the $5d$ level can be calculated in the same way, or it can be calculated via the energy difference

between the $4f$ and $5d$ level by

$$\text{HRBE}(5d) - \text{HRBE}(4f) = E_{\text{tot}}[\text{Ln}^{2+}(4f^{n-1}5d)]$$
$$- E_{\text{tot}}[\text{Ln}^{2+}(4f^n)], \quad (10)$$

which equals the $4f \leftrightarrow 5d$ transition energy of Ln^{2+} (arrow b in Fig. 5). Then the so-defined $5d$ level is higher than the $4f$ level by the zero-phonon energy of transition from the $4f^n$ ground state to the lowest high-spin $4f^{n-1}5d$ state. Hence, the position of the $5d$ level relative to the CBM equals the minimum energy required to adiabatically ionize an electron from the lowest $4f^{n-1}5d$ state to the CB (arrow c in Fig. 5).

The HRBEs of the $4f$ and $5d$ levels of divalent lanthanide ions (Fig. 5) are calculated with the $\text{GGA} + U$ and PBE0-α methods. For comparison, we have also plotted the semiempirical curves obtained by Dorenbos' semiempirical model [10], which makes use of the experimental CT energy of Eu^{3+} (4.56 eV, obtained from the 272 nm CT band peak [3]) and the experimental onset energy of the $4f \leftrightarrow 5d$ transition of Eu^{2+} (3.41 eV [38]) doped in SrB_4O_7. The semiempirical curves have been shifted downward uniformly by 0.80 eV (Fig. S10 within the Supplemental Material [22]), which is the difference between the two total energies of the Ln^{2+} defect calculated at $\text{Ln}_{\text{Sr}}^{\bullet}$ and $\text{Ln}_{\text{Sr}}^{\times}$ equilibrium structures. All the states involved in Fig. 5 are properly occupied except the $4f^{n-1}5d$ states of Pr^{2+} to Sm^{2+} and the $4f^n$ states of La^{2+}, Ce^{2+}, and Gd^{2+} with the PBE0-α method due to the failure of the constrained occupancy approach, and the local lattice structures of each defect are listed in Figs. S2–S7 within the Supplemental Material [22].

The $4f$ levels calculated with the $\text{GGA} + U$ method are approximately 0.5 eV lower on average compared with Dorenbos' semiempirical model, while the $5d$ levels are generally higher by 0.4 eV. For the results calculated with the PBE0-α method, the $5d$ levels are $\lesssim 0.2$ eV different from those of Dorenbos' semiempirical model, and the left half (Pr, Nd, Pm, Sm, and Eu) of the $4f$ levels are $\lesssim 0.1$ eV different from those of Dorenbos' semiempirical model, while the right half (Tb, Dy, Ho, Er, Tm, and Yb) are approximately 0.7 eV higher on average. It shows that the PBE0-α method overestimates the $4f$ levels when the $4f$ shell is more than half full.

Overall, the HRBE obtained here by the first-principles calculations is consistent with the results obtained by Dorenbos' semiempirical model. Furthermore, the calculations in obtaining the trends are based on the generally accepted and formalized DFT method without parameters from experiments, and the closeness of the trends between the PBE0-α method and the less computationally demanding $\text{GGA} + U$ method indicates the appropriateness for high-throughput calculations with the $\text{GGA} + U$ method.

IV. CONCLUSIONS

The band structure, intrinsic defects, and the defects introduced by lanthanide dopants, as well as their stabilities and CTLs, have been thoroughly studied via first-principles calculations based on the PBEsol exchange-correlation functional with the $\text{GGA} + U$ and PBE0-α methods. By comparing the CTLs of different lanthanides with the equilibrium Fermi level in the doped SrB_4O_7 host, the mechanisms of self-reduction are revealed. The results show that the Eu, Sm, and Yb doped in SrB_4O_7 can be reduced from trivalent to divalent in the air atmosphere without any reducing agent, owing to the lower formation energy of divalent lanthanide defects than that of trivalent ones.

The CT transition energies, alternatively the defect levels, of lanthanides are obtained by formalized DFT calculations without resorting to experimental data, and show the same trends as the results obtained by Dorenbos' semiempirical model [9]. This shows that the first-principles calculations based on DFT using the PAW pseudopotentials can be applied to predict certain ground-state and CT properties of lanthanides, provided that the spin-orbit coupling is included and a systematic correction to the band edges is taken into account. Our study here may inspire further revelations of the mechanisms, which will benefit the design and optimization of lanthanide-doped optical materials.

[1] Z. Pei, Q. Su, and J. Zhang, The valence change from RE^{3+} to RE^{2+} ($\text{RE} \equiv$ Eu, Sm, Yb) in SrB_4O_7: RE prepared in air and the spectral properties of RE^{2+}, J. Alloys Compd. **198**, 51 (1993).

[2] Z. Pei, Q. Zeng, and Q. Su, The application and a substitution defect model for $\text{Eu}^{3+} \rightarrow \text{Eu}^{2+}$ reduction in non-reducing atmospheres in borates containing BO_4 anion groups, J. Phys. Chem. Solids **61**, 9 (2000).

[3] H. Liang, H. He, Q. Zeng, S. Wang, Q. Su, Y. Tao, T. Hu, W. Wang, T. Liu, J. Zhang, and X. Hou, VUV and Eu–L_3 edge XANES spectra of europium-doped strontium tetraborate prepared in air, J. Electron Spectrosc. Relat. Phenom. **124**, 67 (2002).

[4] R. Stefani, A. Maia, E. Teotonio, M. Monteiro, M. Felinto, and H. Brito, Photoluminescent behavior of $\text{SrB}_4\text{O}_7:RE^{2+}$ (RE = Sm and Eu) prepared by Pechini, combustion and ceramic methods, J. Solid State Chem. **179**, 1086 (2006).

[5] P. Woźny, M. Runowski, and S. Lis, Influence of boric acid/Sr^{2+} ratio on the structure and luminescence properties (colour tuning) of nano-sized, complex strontium borates doped with Sm^{2+} and Sm^{3+} ions, Opt. Mater. (Amsterdam) **83**, 245 (2018).

[6] J. R. Peterson, W. Xu, and S. Dai, Optical properties of divalent thulium in crystalline strontium tetraborate, Chem. Mater. **7**, 1686 (1995).

[7] W. Xu and J. Peterson, Stabilization of divalent neodymium (Nd^{2+}) in strontium tetraborate, J. Alloys Compd. **249**, 213 (1997).

[8] W. Xu and J. Peterson, Emission from divalent dysprosium (Dy^{2+}) in crystalline strontium tetraborate, Chinese J. Lumin. **22**, 367 (2001).

[9] P. Dorenbos, Modeling the chemical shift of lanthanide $4f$ electron binding energies, Phys. Rev. B **85**, 165107 (2012).

[10] P. Dorenbos, Improved parameters for the lanthanide $4f^q$ and $4f^{q-1}5d$ curves in HRBE and VRBE schemes that takes the nephelauxetic effect into account, J. Lumin. **222**, 117164 (2020).

[11] J. Kapeghian and A. S. Botana, Electronic structure and magnetism in infinite-layer nickelates RNiO$_2$ (R = La–Lu), Phys. Rev. B **102**, 205130 (2020).

[12] K. Hoang, Rare-earth defects in GaN: A systematic investigation of the lanthanide series, Phys. Rev. Mater. **6**, 044601 (2022).

[13] P. E. Blöchl, Projector augmented-wave method, Phys. Rev. B **50**, 17953 (1994).

[14] G. Kresse and D. Joubert, From ultrasoft pseudopotentials to the projector augmented-wave method, Phys. Rev. B **59**, 1758 (1999).

[15] C. G. Van de Walle and J. Neugebauer, First-principles calculations for defects and impurities: Applications to III-nitrides, J. Appl. Phys. **95**, 3851 (2004).

[16] T. R. Durrant, S. T. Murphy, M. B. Watkins, and A. L. Shluger, Relation between image charge and potential alignment corrections for charged defects in periodic boundary conditions, J. Chem. Phys. **149**, 024103 (2018).

[17] C. Freysoldt, B. Grabowski, T. Hickel, J. Neugebauer, G. Kresse, A. Janotti, and C. G. Van de Walle, First-principles calculations for point defects in solids, Rev. Mod. Phys. **86**, 253 (2014).

[18] G. Kresse and J. Hafner, *ab initio* molecular dynamics for liquid metals, Phys. Rev. B **47**, 558 (1993).

[19] G. Kresse and J. Hafner, *ab initio* molecular-dynamics simulation of the liquid-metal–amorphous-semiconductor transition in germanium, Phys. Rev. B **49**, 14251 (1994).

[20] J. P. Perdew, A. Ruzsinszky, G. I. Csonka, O. A. Vydrov, G. E. Scuseria, L. A. Constantin, X. Zhou, and K. Burke, Restoring the Density-Gradient Expansion for Exchange in Solids and Surfaces, Phys. Rev. Lett. **100**, 136406 (2008).

[21] J. P. Perdew, K. Burke, and M. Ernzerhof, Generalized Gradient Approximation Made Simple, Phys. Rev. Lett. **77**, 3865 (1996).

[22] See Supplemental Material at http://link.aps.org/supplemental/10.1103/PhysRevB.107.075145 for the detailed information on the impact of k samplings, kinetic energy cutoffs, difference in the PBE0-α results between those using GGA + U and those using fully-relaxed structures, the spin-orbit coupling correction, the alignment of the VBM, the local structure changes with lanthanides, the dependence of local structures and CTLs on the U values of GGA + U, and the relaxation energy.

[23] L. Wang, T. Maxisch, and G. Ceder, Oxidation energies of transition metal oxides within the GGA + U framework, Phys. Rev. B **73**, 195107 (2006).

[24] Z. Yuan and N. Li, Manipulating the magnetic moment in phosphorene by lanthanide atom doping: A first-principle study, RSC Adv. **6**, 92048 (2016).

[25] C. N. M. Ouma, K. O. Obodo, M. Braun, and G. O. Amolo, *ab initio* insights on the effect of embedding lanthanide atoms on nitrogenated holey doped graphene (g-C$_2$N), J. Mater. Chem. C **6**, 4015 (2018).

[26] J. P. Perdew, M. Ernzerhof, and K. Burke, Rationale for mixing exact exchange with density functional approximations, J. Chem. Phys. **105**, 9982 (1996).

[27] J. He and C. Franchini, Screened hybrid functional applied to $3d^0 \rightarrow 3d^8$ transition-metal perovskites LaMO$_3$ (M = Sc–Cu): Influence of the exchange mixing parameter on the structural, electronic, and magnetic properties, Phys. Rev. B **86**, 235117 (2012).

[28] S. Baroni and R. Resta, *ab initio* calculation of the macroscopic dielectric constant in silicon, Phys. Rev. B **33**, 7017 (1986).

[29] M. Gajdoš, K. Hummer, G. Kresse, J. Furthmüller, and F. Bechstedt, Linear optical properties in the projector-augmented wave methodology, Phys. Rev. B **73**, 045112 (2006).

[30] C.-K. Duan and P. A. Tanner, What use are crystal field parameters? A chemist's viewpoint, J. Phys. Chem. A **114**, 6055 (2010).

[31] J. P. Elliott, B. R. Judd, W. A. Runciman, and M. H. L. Pryce, Energy levels in rare-earth ions, Proc. R. Soc. London A **240**, 509 (1957).

[32] A. Perloff and S. Block, The crystal structure of the strontium and lead tetraborates, SrO·2B$_2$O$_3$ and PbO·2B$_2$O$_3$, Acta Crystallogr. **20**, 274 (1966).

[33] Y. S. Oseledchik, A. L. Prosvirnin, A. I. Pisarevskiy, V. V. Starshenko, V. V. Osadchuk, S. P. Belokrys, N. V. Svitanko, A. S. Korol, S. A. Krikunov, and A. F. Selevich, New nonlinear optical crystals: Strontium and lead tetraborates, Opt. Mater. (Amsterdam) **4**, 669 (1995).

[34] F. Pan, G. Shen, R. Wang, X. Wang, and D. Shen, Growth, characterization and nonlinear optical properties of SrB$_4$O$_7$ crystals, J. Cryst. Growth **241**, 108 (2002).

[35] W.-D. Stein, J. Liebertz, P. Becker, L. Bohatý, and M. Braden, Structural investigations of the tetraborates MB$_4$O$_7$ (M = Pb, Sr, Ba), Eur. Phys. J. B **85**, 236 (2012).

[36] V. Petrov, F. Noack, D. Shen, F. Pan, G. Shen, X. Wang, R. Komatsu, and V. Alex, Application of the nonlinear crystal SrB$_4$O$_7$ for ultrafast diagnostics converting to wavelengths as short as 125 nm, Opt. Lett. **29**, 373 (2004).

[37] A. Tuomela, M. Zhang, M. Huttula, S. Sakirzanovas, A. Kareiva, A. I. Popov, A. P. Kozlova, S. A. Aravindh, W. Cao, and V. Pankratov, Luminescence and vacuum ultraviolet excitation spectroscopy of samarium doped SrB$_4$O$_7$, J. Alloys Compd. **826**, 154205 (2020).

[38] A. Meijerink, J. Nuyten, and G. Blasse, Luminescence and energy migration in (Sr,Eu)B$_4$O$_7$, a system with a $4f^7$–$4f^65d$ crossover in the excited state, J. Lumin. **44**, 19 (1989).

[39] V. Wang, N. Xu, J.-C. Liu, G. Tang, and W.-T. Geng, VASPKIT: A user-friendly interface facilitating high-throughput computing and analysis using VASP code, Comput. Phys. Commun. **267**, 108033 (2021).

[40] K. Momma and F. Izumi, *VESTA3* for three-dimensional visualization of crystal, volumetric and morphology data, J. Appl. Crystallogr. **44**, 1272 (2011).